Ozone Loss and Recovery and the Preconditioning of Upward-Propagating Planetary Wave Activity

JOHN R. ALBERS AND TERRENCE R. NATHAN

Atmospheric Science Program, Department of Land, Air, and Water Resources, University of California, Davis, Davis, California

(Manuscript received 22 September 2012, in final form 29 May 2013)

ABSTRACT

A mechanistic chemistry–dynamical model is used to evaluate the relative importance of radiative, photochemical, and dynamical feedbacks in communicating changes in lower-stratospheric ozone to the circulation of the stratosphere and lower mesosphere. Consistent with observations and past modeling studies of Northern Hemisphere late winter and early spring, high-latitude radiative cooling due to lower-stratospheric ozone depletion causes an increase in the modeled meridional temperature gradient, an increase in the strength of the polar vortex, and a decrease in vertical wave propagation in the lower stratosphere. Moreover, it is shown that, as planetary waves pass through the ozone loss region, dynamical feedbacks precondition the wave, causing a large increase in wave amplitude. The wave amplification causes an increase in planetary wave drag, an increase in residual circulation downwelling, and a weaker polar vortex in the upper stratosphere and lower mesosphere. The dynamical feedbacks responsible for the wave amplification are diagnosed using an ozone-modified refractive index; the results explain recent chemistry–coupled climate model simulations that suggest a link between ozone depletion and increased polar downwelling. The effects of future ozone recovery are also examined and the results provide guidance for researchers attempting to diagnose and predict how stratospheric climate will respond specifically to ozone loss and recovery versus other climate forcings including increasing greenhouse gas abundances and changing sea surface temperatures.

1. Introduction

Global-mean lower-stratospheric temperatures cooled by approximately 0.3–0.5 K decade^{-1} between 1980 and 2000 (WMO 2011). Thompson and Solomon (2009) suggest that many of the temporal features of this cooling trend can be explained as the superposition of three competing effects: long-term stratospheric cooling, transient warming due to aerosols from volcanic eruptions, and transient cooling due to ozone loss associated with volcanic eruptions. Complicating this view, however, is the fact that stratospheric temperature trends have not proceeded uniformly across all latitudes and seasons. For example, poleward of 60°N, the lower stratosphere has exhibited a significant cooling trend between late February and April, a weak cooling trend between May and November, and a warming trend between December and January [see Figs. 4–7 in WMO (2011)].

The springtime cooling trend observed in the Northern Hemisphere (NH) polar lower stratosphere has been reproduced in many modeling studies (e.g., Ramaswamy et al. 2001; Manzini et al. 2003). Part of this springtime cooling trend can be attributed to the radiative response of the atmosphere to increasing abundance of well-mixed greenhouse gasses (GHGs) and decreasing abundance of stratospheric ozone due to ozone-depleting substances. In short, an increase in GHG abundance increases longwave radiative cooling rates in the stratosphere (Brasseur and Hitchman 1988), while decreases in ozone abundance decrease local shortwave solar-heating rates (Brasseur and Solomon 2005). The radiative cooling produced by changes in the abundances of GHGs and ozone will affect the radiative–photochemical–dynamical interactions that are critical to determining the state of Earth's climate system.

In this study we examine the fundamental physics associated with past lower-stratospheric ozone loss and future ozone recovery and how that physics controls the radiative, photochemical, and dynamical feedbacks that affect the structure and circulation of the middle atmosphere. Central to understanding these feedbacks is the ratio of dynamical to photochemical time scales, which

Corresponding author address: John R. Albers, Dept. of Land, Air, and Water Resources, Hoagland Hall, University of California, Davis, Davis, CA 95616-8627.
E-mail: albersjohn@hotmail.com

DOI: 10.1175/JAS-D-12-0259.1

increases by about three orders of magnitude from the lower to the upper stratosphere (Nathan and Cordero 2007, their Fig. 3). Such a dramatic height-dependent change in the ratio of dynamical to photochemical processes has important consequences for the response of the stratosphere to changes in ozone and GHG abundances. To see this, consider first the upper stratosphere, where, owing to the temperature dependence of the gas-phase ozone loss reactions, a negative temperature perturbation causes a positive ozone perturbation (Craig and Ohring 1958; Barnett et al. 1975). This means that a decrease in upper-stratospheric temperature—which is caused by the combined effects of ozone loss and increased GHG abundance—will produce an increase in ozone production; this in turn will cause an increase in the local radiative heating rate. The net result is a negative photochemical feedback that buffers the initial decrease in temperature and ozone.

In contrast to the upper stratosphere, the temperature dependence of the ozone loss reactions in the lower stratosphere is relatively weak (Brasseur and Solomon 2005), and thus the negative ozone–temperature feedback described above is also relatively weak. Nevertheless, if temperatures become cold enough and ozone-depleting substances are present, a positive photochemical feedback causing ozone loss and further depressed temperatures is still possible due to heterogeneous chemistry on polar stratospheric clouds. This feedback is particularly important in the Southern Hemisphere (SH) during spring (Solomon, 1999) but is also important in the NH spring following particularly cold winter seasons (Jin et al. 2006; Manney et al. 2011). While the above photochemical feedbacks are reasonably well understood, the dynamical feedback response to variations in GHGs and ozone is not.

For example, several authors (e.g., Coy et al. 1997; Newman et al. 2001; Hu and Tung 2003) have suggested a positive dynamical feedback mechanism in which observed high-latitude NH late winter and early spring cooling due to ozone loss strengthens the polar vortex. The strengthened polar vortex reduces the vertical propagation of planetary waves (Charney and Drazin 1961), resulting in further cooling and thus further strengthening of the vortex. This view is supported by chemistry–coupled climate models (CCMs) that show that times of increased cooling due to lower-stratospheric ozone loss in the high-latitude NH are accompanied by an increase in the lower-stratospheric meridional temperature gradient, an increase in the strength of lower-stratospheric polar vortex, a decrease in stratospheric vertical wave fluxes, and a decrease in lower-stratospheric polar downwelling (Manzini et al. 2003; Oman et al. 2009). In addition to the changes in the lower stratosphere, ozone depletion has also been linked to warming in the polar upper stratosphere and lower mesosphere due to increased gravity and planetary wave–driven downwelling (Manzini et al. 2003; Smith et al. 2010). In particular, Manzini et al. found that increased downwelling due to planetary waves extended downward from the lower mesosphere into the middle stratosphere, which provides a possible negative dynamical feedback to the ozone loss–induced radiative cooling of the lower and middle stratosphere.

The planetary wave response found by Manzini et al. (2003), however, prompts the following question: how can lower-stratospheric ozone loss cause a reduction in vertical wave propagation, yet cause an increase planetary wave driving in the upper stratosphere and lower mesosphere? Answering this question is particularly important because planetary wave driving exerts substantial control over the strength of the Arctic polar vortex and the strength of polar downwelling, which itself strongly modulates ozone transport and stratospheric temperatures. Moreover, untangling the various radiative and dynamical feedbacks associated with changes in stratospheric ozone abundances is not only relevant for understanding past variations in Earth's climate but will become increasingly important as rising GHG abundances and recovering stratospheric ozone levels combine to produce competing forcing of stratospheric temperature trends over the next 50 years (Austin et al. 2007). Unfortunately, the ramifications of ozone loss and eventual ozone recovery on the dynamical circulation remain uncertain (Metz et al. 2005; WMO 2011).

In light of the complicated response of the stratosphere to changes in ozone and GHGs, isolating the relative importance of each of the radiative, photochemical, and dynamical feedbacks described above will be important for researchers attempting to predict the future state of Earth's climate system. In this paper, we make progress on this problem by exploring the response of planetary waves to past and future variations in lower-stratospheric ozone. We use a mechanistic coupled chemistry–dynamical model to show how dynamical feedbacks communicate changes in lower-stratospheric ozone upward to the upper stratosphere and lower mesosphere to produce changes in the strength of polar downwelling and the strength of Arctic polar vortex. This result provides a physical explanation for results obtained in CCM simulations by Manzini et al. (2003) and Oman et al. (2009).

We organize the paper as follows. In section 2, we introduce the model and describe the ozone loss and recovery experiments. Section 3 details our numerical results and provides mechanistic explanations for the various dynamical feedbacks that produce the wave and circulation changes associated with ozone loss and recovery. Conclusions follow in section 4.

2. Model and experimental design

a. Chemistry–dynamical model

We seek to identify the physics by which ozone loss or recovery alters the radiative, photochemical, and ozone–dynamical feedbacks that drive the zonal-mean circulation. To do this, we follow Albers and Nathan (2012) and consider a quasigeostrophic chemistry–dynamical model that couples radiative transfer, ozone transport, ozone photochemistry, and the dynamical circulation. The wave equations for potential vorticity, ozone volume mixing ratio, and temperature are as follows:

$$\left(\frac{\partial}{\partial t}+\overline{u}\frac{\partial}{\partial x}\right)q'+\frac{\partial\psi'}{\partial x}\frac{\partial\overline{Q}}{\partial y}=\frac{\kappa f_0}{\rho H}\frac{\partial}{\partial z}\left(\frac{\rho}{N^2}J'\right), \quad (1)$$

$$\left(\frac{\partial}{\partial t}+\overline{u}\frac{\partial}{\partial x}\right)\gamma'+\frac{\partial\psi'}{\partial x}\frac{\partial\overline{\gamma}}{\partial y}+w'\frac{\partial\overline{\gamma}}{\partial z}=S', \quad (2)$$

$$\left(\frac{\partial}{\partial t}+\overline{u}\frac{\partial}{\partial x}\right)\frac{\partial\psi'}{\partial z}-\frac{\partial\psi'}{\partial x}\frac{\partial\overline{u}}{\partial z}+N^2w'/f_0=\frac{\kappa}{Hf_0}J', \quad (3)$$

where the perturbation potential vorticity and basic-state potential vorticity gradient are

$$q'=\nabla^2\psi'+\frac{1}{\rho}\frac{\partial}{\partial z}\left(\frac{\rho f_0^2}{N^2}\frac{\partial\psi'}{\partial z}\right),$$

$$\frac{\partial\overline{Q}}{\partial y}=\beta-\frac{\partial^2\overline{u}}{\partial y^2}-\frac{1}{\rho}\frac{\partial}{\partial z}\left(\frac{\rho f_0^2}{N^2}\frac{\partial\overline{u}}{\partial z}\right).$$

The wave-heating rate and wave-ozone production/destruction rate are, respectively,

$$J'=\left(-\frac{f_0H}{\kappa}\alpha\frac{\partial\psi'}{\partial z}\right)+\left[\Gamma_1\gamma'-\Gamma_2\int_z^\infty\frac{\rho(z')}{\rho_0}\gamma'\,dz'\right], \quad (4)$$

$$S'=-\xi_1\gamma'+\xi_2\int_z^\infty\frac{\rho(z')}{\rho_0}\gamma'(x,y,z,t)\,dz'-\frac{f_0H}{R}\xi_T\frac{\partial\psi'}{\partial z}. \quad (5)$$

The zonal-mean equations for zonal wind, ozone volume mixing ratio, temperature, and meridional circulation are

$$\frac{\partial}{\partial t}\left[\frac{\partial^2\overline{u}}{\partial y^2}+\frac{1}{\rho}\frac{\partial}{\partial z}\left(\frac{\rho f_0^2}{N^2}\frac{\partial\overline{u}}{\partial z}\right)\right]=\frac{\partial^2}{\partial y^2}\left[\frac{1}{\rho}\frac{\partial}{\partial z}\left(\frac{\rho f_0^2}{N^2}\overline{v'\frac{\partial\psi'}{\partial z}}\right)\right]+\frac{1}{\rho}\frac{\kappa}{H}\frac{\partial}{\partial z}\left(\frac{\rho f_0}{N^2}\frac{\partial\overline{J}}{\partial y}\right)-\frac{1}{\rho}\frac{\partial}{\partial z}\left[\frac{\rho f_0^2}{N^2}\alpha\left(\frac{\partial\overline{u}}{\partial z}-\frac{\partial\overline{u}_R}{\partial z}\right)\right], \quad (6)$$

$$\frac{\partial\overline{\gamma}}{\partial t}=-\left(\overline{v}\frac{\partial\overline{\gamma}}{\partial y}+\overline{w}\frac{\partial\overline{\gamma}}{\partial z}\right)-\left[\frac{\partial}{\partial y}(\overline{v'\gamma'})+\frac{1}{\rho}\frac{\partial}{\partial z}(\rho\overline{w'\gamma'})\right]+\overline{S}, \quad (7)$$

$$\frac{\partial\overline{T}}{\partial t}+\frac{HN^2}{R}\overline{w}=-\frac{\partial}{\partial y}(\overline{v'T'})+\frac{1}{c_p}\overline{J}-\alpha(\overline{T}-\overline{T_R}), \quad (8)$$

$$\frac{\partial^2\overline{\chi}}{\partial y^2}+\frac{\rho f_0^2}{N^2}\frac{\partial}{\partial z}\left(\frac{1}{\rho}\frac{\partial\overline{\chi}}{\partial z}\right)=\frac{\rho}{N^2}\left\{\frac{\kappa}{H}\frac{\partial\overline{J}}{\partial y}-\frac{R}{H}\left[\frac{\partial^2(\overline{v'T'})}{\partial y^2}+\alpha\frac{\partial}{\partial y}(\overline{T}-\overline{T}_R)\right]\right\}, \quad (9)$$

where the zonal-mean meridional and vertical velocities are given by

$$(\overline{v},\overline{w})=\left(-\frac{1}{\rho}\frac{\partial\overline{\chi}}{\partial z},\frac{1}{\rho}\frac{\partial\overline{\chi}}{\partial y}\right). \quad (10)$$

The zonal-mean ozone heating rate and ozone production/destruction rate are, respectively,

$$\overline{J}=\Gamma_1(\overline{\gamma}-\overline{\gamma}_R)-\Gamma_2\int_z^\infty\frac{\rho(z')}{\rho_0}(\overline{\gamma}-\overline{\gamma}_R)\,dz', \quad (11)$$

$$\overline{S}=-\xi_1(\overline{\gamma}-\overline{\gamma}_R)+\xi_2\int_z^\infty\frac{\rho(z')}{\rho_0}(\overline{\gamma}-\overline{\gamma}_R)\,dz'-\xi_T(\overline{T}-\overline{T}_R). \quad (12)$$

The subscript R denotes fields that are in radiative and photochemical equilibrium (discussed next). All variables in Eqs. (1)–(12) are defined in Table 1.

b. Radiative–photochemical model

The effects of ozone loss and recovery are incorporated into our model via the radiative–photochemical equilibrium distributions of ozone and temperature [$\overline{\gamma_R}$ and $\overline{T_R}$ in Eqs. (1)–(12)]. To show this, we partition the total ozone and temperature fields as

$$\gamma(x,y,z,t)\doteq\underbrace{\overline{\gamma_R}(y,z)}_{\text{(I)}}+\underbrace{\overline{\delta\gamma_R}(y,z,t)}_{\text{(II)}}+\underbrace{\gamma'(x,y,z,t)}_{\text{(III)}}, \quad (13)$$

$$T(x,y,z,t)\doteq\underbrace{\overline{T_R}(y,z)}_{\text{(I)}}+\underbrace{\overline{\delta T_R}(y,z,t)}_{\text{(II)}}+\underbrace{T'(x,y,z,t)}_{\text{(III)}}, \quad (14)$$

where terms I are the basic-state radiative–photochemical equilibrium distributions of ozone and temperature; terms II are the departures of zonal-mean ozone and

TABLE 1. List of variables.

$t, x, y, z = -H\ln(p/p_0)$	Time and distances in the eastward, northward, and vertical directions
$p(z) = p_0\exp(-z/H), p_0$	Basic-state pressure, reference pressure at the surface of Earth
$\rho(z) = \rho_0\exp(-z/H), \rho_0$	Basic-state density, reference density at the surface of Earth
f_0, β, H	Planetary vorticity, planetary vorticity gradient evaluated at $\theta_0 = 60°$ latitude, and mean scale height (=7 km)
$N^2(z)$	Brunt–Väisälä frequency squared ($=4\times10^{-4}\,\mathrm{s}^{-2}$)
$\kappa = R/C_P$	R is the gas constant and C_p is the specific heat at constant pressure
$\psi', T', \gamma', v', w'$	Perturbation geostrophic streamfunction, temperature, ozone volume mixing ratio, and meridional and vertical winds
$\overline{u}, \overline{T}, \overline{\gamma}$	Zonal-mean zonal wind, temperature, and ozone volume mixing ratio
$\overline{v}, \overline{w}, \overline{\chi}$	Zonal-mean meridional and vertical wind, and zonal-mean meridional streamfunction
$\Gamma_j(z;\overline{\gamma}, \overline{T}, \mu)(j=1,2)$	Radiative–photochemical heating coefficients
$\alpha(z),\ b$	Newtonian cooling coefficients
$\xi_j(z;\overline{\gamma}, \overline{T}, \mu)(j=1,2,T)$	Radiative–photochemical ozone production and destruction coefficients
μ	Solar zenith angle

temperature from radiative–photochemical equilibrium, that is, $\overline{\delta\gamma_R} = \overline{\gamma} - \overline{\gamma_R}$ and $\overline{\delta T_R} = \overline{T} - \overline{T_R}$; and terms III are the wave perturbations in ozone and temperature.

In the absence of dynamics, a balance between ozone radiative heating and longwave thermal emission is the primary determinant of the temperature of the stratosphere (Lindzen and Goody 1965; Brasseur and Solomon 2005). Thus the radiative–photochemical state of the stratosphere can be determined by jointly solving the following equations for ozone and temperature:

$$\frac{\partial\gamma}{\partial t} = 2\frac{J_2 n_2}{n_m} - 2\frac{J_3 k_3(T)}{n_2}\gamma^2 + \Delta_{\mathrm{ODS}}, \tag{15}$$

$$\frac{\partial T}{\partial t} = \frac{q_3 N_0}{m_a c_p}\gamma - \alpha T + b, \tag{16}$$

where J_i, n_i, and k_i are, respectively, the photodissociation rate, number density, and temperature-dependent reaction rate for molecular oxygen ($i = 2$), ozone ($i = 3$), and air ($i = m$); q_3 is the heating rate due to the absorption of solar radiation by ozone; α and b are the Newtonian cooling coefficients; $\Delta_{\mathrm{ODS}}(y, z)$ is an imposed external ozone forcing that represents the effects of ozone loss or recovery; m_a is the molecular weight of air; c_p is the gas constant; and N_0 is Avogadro's number. In addition to standard odd oxygen gas-phase chemistry, the temperature-dependent ozone reaction rate k_3 is parameterized to account for catalytic ozone destruction cycles involving NO_x, HO_x, and ClO_x (Haigh and Pyle 1982). In the absence of ozone loss or recovery ($\Delta_{\mathrm{ODS}} = 0$), Eqs. (15) and (16) reduce to the equations for ozone and temperature first derived by Lindzen and Goody (1965).

We use Eqs. (15) and (16) to derive equations for the partitioned parts of the ozone and temperature fields, that is, terms I, II, and III in Eqs. (13) and (14). We begin by noting that in Eq. (15) $(n_2/n_m) = 0.21$, while n_2 is expanded as (Lindzen and Goody 1965)

$$n_2 \doteq \overline{n_2}\left(1 - \frac{\overline{\delta T_R} + T'}{\overline{T}}\right) \Rightarrow \frac{1}{n_2} = \frac{1}{\overline{n_2}}\left(1 + \frac{\overline{\delta T_R} + T'}{\overline{T}}\right). \tag{17}$$

We also expand $K(T)$ in a Taylor series about $\overline{T_R}$ as

$$K(T) \doteq K(\overline{T_R}) + \left.\frac{dK}{dT}\right|_{\overline{T_R}}(\overline{\delta T_R} + T'), \tag{18}$$

where $K(\overline{T_R}) = (k_3/k_2)\exp[-D/\overline{T_R}]$ and D is the temperature-dependent reaction rate that accounts for catalytic ozone loss cycles involving NO_x, HO_x, and ClO_x [Albers and Nathan 2012, their Eq. (A13)].

Inserting Eqs. (13), (14), (17), and (18) into Eqs. (15) and (16) and ignoring products of perturbations ($\overline{\delta T_R}T', T'^2$, etc.) yields

$$\frac{\partial(\overline{\gamma_R} + \overline{\delta\gamma_R} + \gamma')}{\partial t} = 2\frac{J_2 n_2}{n_m} - 2\frac{J_3 K(\overline{T_R})}{\overline{n_2}}\overline{\gamma_R}^2 + \Delta_{\mathrm{ODS}} - \left[4\frac{J_3 K(\overline{T_R})}{\overline{n_2}}\overline{\gamma_R}\right]\overline{\delta\gamma_R} - \left[2\frac{J_3 K(\overline{T_R})}{\overline{n_2}}\frac{\overline{\gamma_R}^2}{\overline{T_R}}\left(1 + \frac{D}{\overline{T_R}}\right)\right]\overline{\delta T_R}$$
$$- \left[4\frac{J_3 K(\overline{T_R})}{\overline{n_2}}\overline{\gamma_R}\right]\gamma' - \left[2\frac{J_3 K(\overline{T_R})}{\overline{n_2}}\frac{\overline{\gamma_R}^2}{\overline{T_R}}\left(1 + \frac{D}{\overline{T_R}}\right)\right]T', \tag{19}$$

$$\frac{\partial(\overline{T_R}+\overline{\delta T_R}+T')}{\partial t}=\frac{q_3N_0}{m_ac_p}\overline{\gamma_R}-\alpha\overline{T_R}+b+\frac{q_3N_0}{m_ac_p}\overline{\delta\gamma_R}-\alpha\overline{\delta T_R}+\frac{q_3N_0}{m_ac_p}\gamma'-\alpha T'. \tag{20}$$

For steady-state conditions and in the absence of waves, Eqs. (19) and (20) reduce to

$$0=2\frac{J_2n_2}{n_m}-2\frac{J_3K(\overline{T_R})}{\overline{n_2}}\overline{\gamma_R}^2+\Delta_{\mathrm{ODS}}, \tag{21}$$

$$0=\frac{q_3N_0}{m_ac_p}\overline{\gamma_R}-\alpha\overline{T_R}+b. \tag{22}$$

Equations (21) and (22) are used to calculate the radiative–photochemical equilibrium distributions of ozone and temperature ($\overline{\gamma_R}$ and $\overline{T_R}$) in Eqs. (1)–(12), the details of which we defer to section 2c. In Eq. (21) we note that Δ_{ODS} directly affects the equilibrium state of system, so that we can write

$$\overline{\gamma_R}(y,z)=\overline{\gamma_R}^{\mathrm{Clim}}(y,z)+\overline{\gamma_R}^{\mathrm{ODS}}(y,z), \tag{23}$$

$$\overline{T_R}(y,z)=\overline{T_R}^{\mathrm{Clim}}(y,z)+\overline{T_R}^{\mathrm{ODS}}(y,z). \tag{24}$$

In these equations, the superscripts "Clim" and "ODS" denote, respectively, the climatological radiative–photochemical equilibrium distribution and the ozone loss or recovery perturbation. If $\Delta_{\mathrm{ODS}}=0$, then the equilibrium solutions for the ozone and temperature fields simply become the climatological radiative equilibriums.

Subtracting Eqs. (21) and (22) from Eqs. (19) and (20), respectively, and zonally averaging yields the zonal-mean equations for ozone and temperature:

$$\frac{\partial\overline{\gamma}}{\partial t}=-\xi_1(\overline{\gamma}-\overline{\gamma_R})-\xi_T(\overline{T}-\overline{T_R}), \tag{25}$$

$$\frac{\partial\overline{T}}{\partial t}=\Gamma_1(\overline{\gamma}-\overline{\gamma_R})-\alpha(\overline{T}-\overline{T_R}). \tag{26}$$

In Eqs. (25) and (26), $\overline{\delta\gamma_R}=\overline{\gamma}-\overline{\gamma_R}$ and $\overline{\delta T_R}=\overline{T}-\overline{T_R}$ are wave-driven departures from radiative equilibrium.

Subtracting Eqs. (21) and (25) from Eq. (19) and subtracting Eqs. (22) and (26) from Eq. (20) yields the wave equations for ozone and temperature:

$$\frac{\partial\gamma'}{\partial t}=-\xi_1\gamma'-\xi_TT', \tag{27}$$

$$\frac{\partial T'}{\partial t}=\Gamma_1\gamma'-\alpha T'. \tag{28}$$

In Eqs. (25)–(28), the radiative–photochemical parameters are defined by (Albers and Nathan 2012)

$$\xi_1=4\frac{J_3K(\overline{T_R})}{\overline{n_2}}\overline{\gamma_R}, \tag{29}$$

$$\xi_T=2\frac{J_3K(\overline{T_R})}{\overline{n_2}}\frac{\overline{\gamma_R}^2}{\overline{T_R}}\left(1+\frac{D}{\overline{T_R}}\right), \tag{30}$$

$$\Gamma_1=\frac{q_3N_0}{m_ac_p}. \tag{31}$$

In the absence of dynamics, Eqs. (7) and (8) and Eqs. (2) and (3) are equivalent to Eqs. (25) and (26) and Eqs. (27) and (28), respectively. For simplicity, we have ignored the contributions from the shielding terms (ξ_2 and Γ_2) in Eqs. (25)–(28).

ANALYSIS

To most easily expose the physics that describes the temperature and ozone response to ozone-depleting substances, we assume that Δ_{ODS} is small (i.e., Δ_{ODS} is on the order of the linear perturbations rather than on the order of the equilibrium fields). With Δ_{ODS} small, we repeat the previous linearization to obtain

$$\frac{\partial(\overline{\delta\gamma_R})}{\partial t}=-\xi_1\overline{\delta\gamma_R}-\xi_T\overline{\delta T_R}-\Delta_{\mathrm{ODS}}, \tag{32}$$

$$\frac{\partial(\overline{\delta T_R})}{\partial t}=\Gamma_1\overline{\delta\gamma_R}-\alpha\overline{\delta T_R}, \tag{33}$$

where $\xi_1,\xi_T,\Gamma_1,$ and α are all positive. In Eqs. (32) and (33), $\overline{\delta\gamma_R}$ and $\overline{\delta T_R}$ are departures from radiative equilibrium due to the ODS terms (ODSs).

The terms involving ξ_1 and ξ_T represent the relaxation of ozone back to radiative equilibrium, where ξ_T represents the ozone–temperature feedback due to the temperature dependence of the ozone reaction rate [k_3 in Eq. (15)]; Γ_1 represents ozone radiative heating [q_3 in Eq. (16)]; and α represents the relaxation of temperature back to radiative equilibrium [the Newtonian cooling term in Eq. (16)]. To understand the response of ozone and temperature to ODSs, we set the LHS of Eqs. (32) and (33) to zero and solve for $\overline{\delta\gamma_R}$ and $\overline{\delta T_R}$, which yields

$$\overline{\delta\gamma_R}=-\left(\frac{\Gamma_1}{\xi_1\alpha+\xi_T\Gamma_1}\right)\Delta_{\mathrm{ODS}}, \tag{34}$$

$$\overline{\delta T_R}=-\left(\frac{\alpha}{\xi_1\alpha+\xi_T\Gamma_1}\right)\Delta_{\mathrm{ODS}}. \tag{35}$$

These coupled equations describe the ozone and temperature response to imposed ODSs. Shepherd and Jonsson (2008) have lucidly presented a physical interpretation of Eqs. (34) and (35). But in contrast to our study, where Eqs. (34) and (35) have been derived from first principles, they obtained their equations by asserting a physically based set of equations for ozone and temperature. Shepherd and Jonsson's analysis highlights two important points regarding the response of ozone and temperature to ODSs. First, as expected, an increase in ODSs will produce a decrease in ozone and a corresponding decrease in temperature; the temperature response represents the radiative response of temperature to ODSs. Second, in the absence of ξ_T, the change in temperature resulting from ODSs would be larger; this represents the photochemical feedback response of temperature to ODSs. Thus k_3 buffers both the loss in ozone and the decrease in temperature due to ODSs; this is simply the inverse temperature–ozone phase relationship first discussed by Craig and Ohring (1958). In our model, the radiative and photochemical feedbacks just described are incorporated into our prognostic equations via the radiative equilibrium basic states ($\overline{\gamma_R}$ and $\overline{T_R}$).

c. Experiments

Solutions to Eqs. (1)–(12) are sought in the form of highly truncated Fourier series, where we write the planetary wave, zonal-mean fields, and radiative–photochemical coefficients each as a single Fourier mode:

$$(\psi', \gamma', w') = [\Psi(z,t), \gamma_0'(z,t), w_0'(z,t)]e^{z/2H}e^{ikx}\sin(ly) + \text{c.c.}, \tag{36a}$$

$$(\overline{u}, \overline{v}, \overline{\chi}) = [U_0(z,t), \overline{v}_0(z,t), \overline{\chi}_0(z,t)]\sin(ly), \tag{36b}$$

$$\overline{w} = \overline{w}_0(z,t)\cos(ly), \tag{36c}$$

$$(\overline{\gamma}, \overline{T}) = [\overline{\gamma}_0(z,t), \overline{T}_0(z,t)] + [\overline{\gamma}_1(z,t), \overline{T}_1(z,t)]\cos(ly), \tag{36d}$$

$$(\Gamma_i, \xi_i, \xi_T) = [\Gamma_{i,0}(z), \xi_{i,0}(z), \xi_{T,0}] + [\Gamma_{i,1}, \xi_{i,1}, \xi_{T,1}]\cos(ly), i = 1, 2. \tag{36e}$$

Equations governing the time–height evolution of the wind, temperature, and ozone fields are formed by inserting Eqs. (36) into Eqs. (1)–(12) and projecting onto $\sin(ly)$ and $\cos(ly)$.

We present three sets of experiments. The first (baseline) experiment (O_3-Clim) is initialized using climatological profiles of ozone, temperature, and zonal-mean wind representative of late winter and early spring. In the second (O_3-Loss) and third (O_3-Recov) experiments, we impose zonal-mean ozone perturbations representative of ozone depletion due to heterogeneous chemistry (Jin et al. 2006) or predicted decadal ozone recovery (Li et al. 2009), respectively. For the climatological ozone profiles, we use the data of Keating et al. (1996), who aggregate ozone observations between around 1960 and the mid-1980s. The Keating et al. ozone data provide a natural baseline to compare with our experiments, which examine the ozone loss events that occurred in the 2000s (Jin et al. 2006) and eventual ozone recovery that is expected to occur by around 2050 (Li et al. 2009). Thus O_3-Loss represents the lowest ozone concentration, O_3-Clim represents an intermediate concentration, and O_3-Recov represents the highest concentration.

For each experiment we first calculate the equilibrium profiles for zonal-mean temperature and ozone at 40°, 60°, and 80°N for climatological conditions ($\overline{\gamma}_{0,R}$ and $\overline{T}_{0,R}$) using Eqs. (21) and (22) with $\Delta_{\text{ODS}} = 0$. The climatological radiative equilibrium profiles for the meridional gradients of ozone and temperature at midchannel are then calculated as

$$\overline{\gamma}_{1,R} = -\frac{1}{l}\frac{\partial\overline{\gamma}_R}{\partial y} = -\frac{1}{l}\frac{[\overline{\gamma}_{0,R}(80°) - \overline{\gamma}_{0,R}(40°)]}{\delta y}, \tag{37}$$

$$\overline{T}_{1,R} = -\frac{1}{l}\frac{\partial\overline{T}_R}{\partial y} = -\frac{1}{l}\frac{[\overline{T}_{0,R}(80°) - \overline{T}_{0,R}(40°)]}{\delta y}, \tag{38}$$

where $l = \pi/a_e$.

When $\Delta_{\text{ODS}} \neq 0$, we have two options for calculating the equilibrium solutions. The first option would be to explicitly specify Δ_{ODS}, which would require detailed knowledge of the chemistry and physics involved in ozone depletion due to ODSs and polar stratospheric clouds. This knowledge would allow us to calculate the equilibrium solutions using Eqs. (21) and (22). The second simpler option is to specify $\overline{\gamma_R}^{\text{ODS}}$ in Eq. (23) consistent with observations. In this case, we insert Eq. (23) into Eq. (22) and solve for the new equilibrium temperature field [Eq. (24)], where Δ_{ODS} can now be implicitly calculated if so desired.

For the ozone loss perturbation ($\overline{\gamma_R}^{\text{ODS}}$), we use data taken from Jin et al. (2006), who computed observed ozone losses from 50° to 80°N between 1 January and 26 March. For consistency with the Jin et al. data, and because we are interested in the effects of extratropical ozone recovery, we use the data of Li et al. (2009) between 50° and 80°N for the ozone recovery perturbation. For both the ozone loss and recovery experiments,

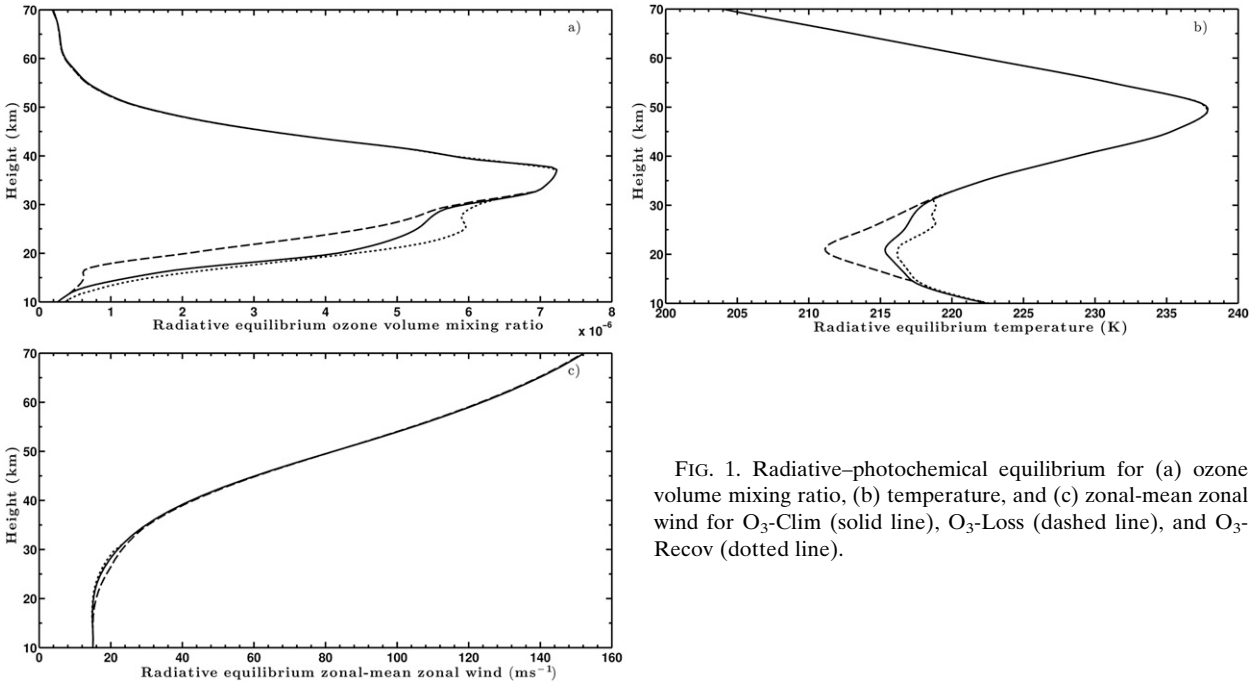

FIG. 1. Radiative–photochemical equilibrium for (a) ozone volume mixing ratio, (b) temperature, and (c) zonal-mean zonal wind for O_3-Clim (solid line), O_3-Loss (dashed line), and O_3-Recov (dotted line).

the imposed ozone perturbation is zero above about 30 km and at 40°N. Given the radiative equilibrium distributions of temperature, we then determine the climatological, ozone loss, and ozone recovery radiative equilibrium zonal-mean winds by the thermal wind relation

$$\overline{U}_{0,R} = -\frac{R}{f_0 H}\int_{z_B}^{z_T}\frac{\partial \overline{T}}{\partial y}\,dz + \overline{U}_{0,z_B} = \frac{Rl}{f_0 H}\int_{z_B}^{z_T}\overline{T}_{1,R}\,dz + \overline{U}_{0,z_B}, \tag{39}$$

where we have assumed $\overline{U}_0(z_B) = 15\ \mathrm{m\,s^{-1}}$. Figures 1a–c show the radiative photochemical equilibrium distributions of ozone volume mixing ratio, temperature, and zonal-mean zonal wind for the climatological, ozone loss, and ozone recovery experiments, respectively.

Equations (1)–(12) are solved using the same boundary conditions as in Albers and Nathan (2012). The initial conditions for all of the prognostic fields are set equal to their radiative equilibrium values and we use a solar zenith angle representative of March to coincide with the observed NH late winter–early spring maximum in lower-stratospheric ozone loss and minimum in lower-stratospheric temperature (WMO 2011). We carried out model simulations for planetary waves 1 ($n = 1$) and 2 ($n = 2$) and the results are qualitatively similar. The results presented later are for planetary wave 1. For all of the experiments, the model is run until a steady state is reached and the model results are then compared.

We have designed the experiments to isolate the physics associated with the effect of episodic lower-stratospheric ozone loss events and decadal lower-stratospheric ozone recovery on the zonal-mean circulation of the stratosphere. Our experiments are motivated in part by Oman et al. (2009), who showed that lower-stratospheric ozone loss was far more important for generating changes in wave driving and the Brewer–Dobson circulation than changes in upper-stratospheric ozone loss. Examination of major ozone loss events is also motivated by evidence that over the last 40 years, the coldest stratospheric winters in the Arctic have been getting progressively colder, particularly during the late winter and early spring (Pawson and Naujokat 1999; Rex et al. 2006; Tilmes et al. 2006). This fact is highlighted by recent record-breaking NH polar ozone loss events in 2005 (Jin et al. 2006) and 2011 (Manney et al. 2011).

d. Diagnostics

To evaluate the relative importance of the radiative, photochemical, and dynamical feedbacks involved in communicating changes in lower-stratospheric ozone to the circulation of the stratosphere and lower mesosphere, we consider steady-state conditions so that the zonal-mean wind equation [Eq. (6)] becomes

$$0 = \underbrace{\frac{\partial^2}{\partial y^2}\left[\frac{1}{\rho}\frac{\partial}{\partial z}\left(\frac{\rho f_0^2}{N^2}\overline{\nu'\frac{\partial \psi'}{\partial z}}\right)\right]}_{\overline{u}_{\mathrm{PWD}}} + \underbrace{\frac{1}{\rho}\frac{\kappa}{H}\frac{\partial}{\partial z}\left(\frac{\rho f_0}{N^2}\frac{\partial \overline{J}}{\partial y}\right)}_{\overline{u}_{\mathrm{OH}}} \underbrace{- \frac{1}{\rho}\frac{\partial}{\partial z}\left[\frac{\rho f_0^2}{N^2}\alpha\left(\frac{\partial \overline{u}}{\partial z} - \frac{\partial \overline{u}_R}{\partial z}\right)\right]}_{\overline{u}_{\mathrm{NC}}}. \quad (40)$$

Equation (40) shows that the steady-state zonal-mean wind is determined by a three-way balance between zonal-mean wind forcing mechanisms originating from planetary wave drag $\overline{u}_{\mathrm{PWD}}$, ozone heating $\overline{u}_{\mathrm{OH}}$, and Newtonian cooling $\overline{u}_{\mathrm{NC}}$. The planetary wave drag term is a function of zonally asymmetric ozone via wave–ozone heating [Eq. (4)], while the ozone heating term is a function of both zonal-mean ozone (ZMO) and zonally asymmetric ozone (ZAO) due to ozone transports, wave–ozone flux convergences, and production/destruction of ozone in Eq. (7). The Newtonian cooling term represents the relaxation of the zonal-mean wind toward radiative equilibrium due to longwave thermal emission.

The radiative, photochemical, and dynamical feedback responses of the zonal-mean wind to ozone loss and recovery are all manifest in Eq. (40). In particular, ozone loss and recovery affect Eq. (40) radiatively in two ways: first, $\overline{u}_{\mathrm{OH}}$ is modified via changes to $\overline{\gamma}_R$ that modulate the zonal-mean heating rate both directly [Eq. (11)] and indirectly [Eq. (12)]; and second, $\overline{u}_{\mathrm{NC}}$ is modified via changes to $\overline{U}_R$ {which is related to $\overline{T}_R$ via the thermal wind relationship [Eq. (39)]}. Photochemical feedbacks affect Eq. (40) by modifying $\overline{u}_{\mathrm{OH}}$ via changes in ZMO heating [Eq. (11)] due to temperature-dependent chemistry [the third term on the RHS of Eq. (12)]. Dynamical feedbacks affect Eq. (40) by modifying $\overline{u}_{\mathrm{OH}}$ via ozone flux convergences [the second bracket of terms on the RHS of Eq. (7)] and by modifying $\overline{u}_{\mathrm{PWD}}$ via changes in wave propagation and damping. The physics governing the radiative, photochemical, and dynamical feedbacks described above, which vary strongly with altitude, are discussed in detail in Albers and Nathan (2012, their Fig. 2). Because the dynamical feedbacks are central to this study, we summarize them next.

Albers and Nathan (2012, their Fig. 1) showed that ZAO operates along two pathways that combine to affect the zonal-mean circulation in the stratosphere. One pathway involves ZAO-modulated planetary wave drag and the other ZAO-modulated ozone flux convergences. Most importantly, Albers and Nathan showed that dynamical feedbacks alter both wave damping and wave propagation to ''precondition'' the planetary wave amplitudes in the lower stratosphere. As the preconditioned waves leave the lower stratosphere and propagate into the middle stratosphere to lower mesosphere, their amplitudes are sufficiently altered to cause significant changes in planetary wave drag and the zonal-mean circulation. This preconditioning process is central to our study, because it provides a physical mechanism for understanding how the effects of lower-stratospheric ozone perturbations are propagated upward into the middle and upper stratosphere.

To understand how imposed changes in ozone produce changes in planetary wave driving of the zonal-mean circulation, we use the expression for the ozone-modified divergence of Eliassen–Palm (EP) flux derived by Nathan and Cordero [2007; their Eq. (1)]:

$$\nabla \cdot F \propto -|A|^2 m_r m_i \exp\int_0^z (-m_i)\, dz'. \quad (41)$$

In Eq. (41), $m = m_r + im_i$ is the complex, ozone-modified refractive index, where m_r and m_i measure wave propagation and wave damping, respectively; and A is the Wentzel–Kramers–Brillouin (WKB) wave amplitude, which also depends on m_r and m_i. Both m_i and m_r, which are defined in Nathan and Cordero (2007), are functions of ZMO, ZAO, and Newtonian cooling. For the numerical results, we evaluate wave propagation by

$$m_0^2 = N^2\left[\overline{u}^{-1}\frac{\partial \overline{Q}}{\partial y} - (k^2 + l^2)\right] - \frac{1}{4H^2}, \quad (42)$$

where m_0 is the lowest-order approximation to m_r, which corresponds to the classical one-dimensional refractive index of Charney and Drazin (1961). We measure changes in wave damping by the numerically calculated streamfunction amplitude modulus, which is related to the WKB amplitude to lowest order as

$$|\psi'|^2 \propto |A|^2 \exp\left(-2\int_0^z m_i\, dz'\right)^2. \quad (43)$$

In addition to the steady-state zonal wind and planetary wave diagnostics listed above, we also measure the effect of dynamical feedbacks on the zonal-mean circulation using the transformed Eulerian mean (TEM) residual vertical velocity. In the steady state, the TEM vertical velocity is given by (Holton 2004)

$$\overline{w}^* = -\rho^{-1}\frac{\partial}{\partial y}\left(f_0^{-1}\int_z^\infty \nabla \cdot F\, dz'\right), \quad (44)$$

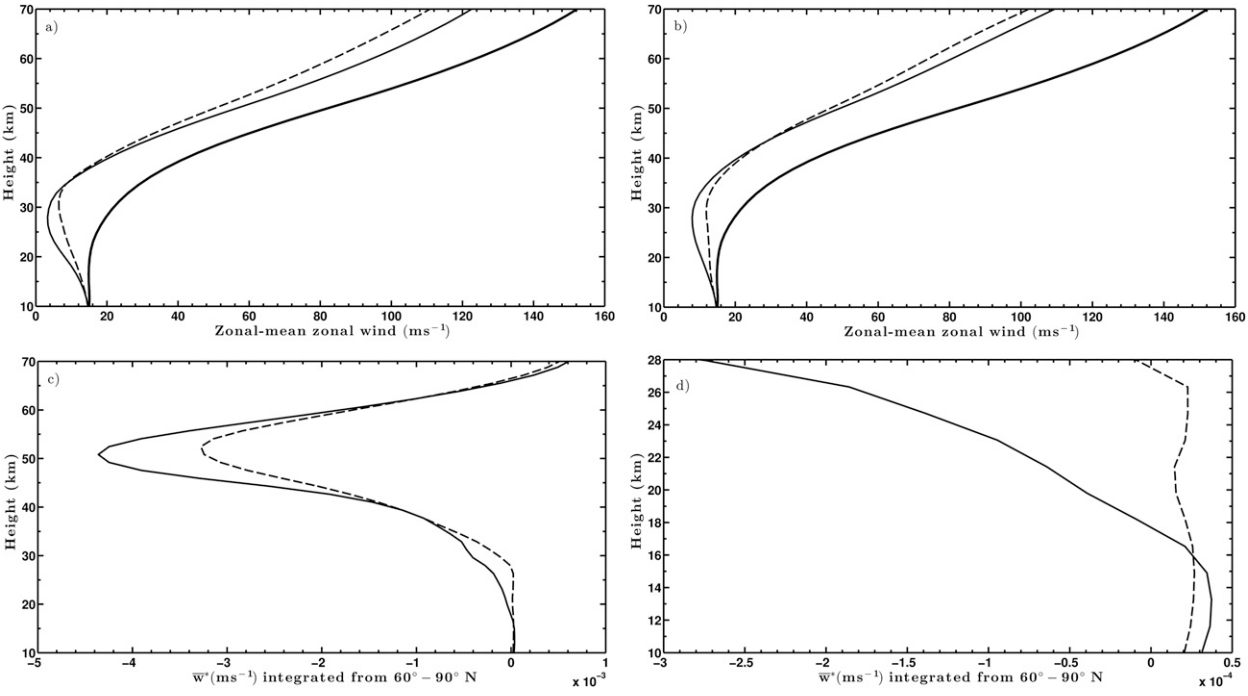

FIG. 2. Steady-state zonal-mean zonal wind for O_3-Clim (solid) and O_3-Loss (dashed) when (a) ZAO and ZMO are included in the model and (b) only ZMO is included in the model. The thick solid line denotes the radiative equilibrium zonal-mean zonal wind. (c),(d) The difference (O_3-Clim minus O_3-Loss) in the area-integrated residual vertical velocity when ZAO and ZMO are included in the model (solid line) and when only ZMO is included in the model (dashed line). The vertical axis of (d) is enlarged in order to show detail in the lowermost stratosphere.

where in our one-dimensional (in height) model framework, $\nabla \cdot F$ is due solely to the vertical convergence of the northward heat flux.

3. Numerical experiments

We now compare the climatological (O_3-Clim), lower-stratospheric ozone loss (O_3-Loss), and ozone recovery (O_3-Recov) experiments (see section 2 for details). We also run each of the experiments with ZAO suppressed in order to isolate the role of ZAO in communicating the lower-stratospheric ozone perturbations upward into the interior of the stratosphere.

a. Results

1) LOWER-STRATOSPHERIC OZONE LOSS

We begin by comparing our results to the March ozone loss results of Manzini et al. (2003, their Figs. 9 and 10). Manzini et al.'s results provide five benchmarks for comparison: 1) a 1–4 m s^{-1} increase in the zonal-mean wind between about 10 and 40 km; 2) a 1–4 m s^{-1} decrease in the zonal-mean wind between about 40 and 70 km; 3) a roughly 0–0.25 mm s^{-1} decrease in the TEM residual vertical velocity between about 10 and 30 km (a decrease in downwelling); 4) a 0–0.5 mm s^{-1} increase in the TEM residual vertical velocity between about 30 and 70 km (an increase in downwelling); and 5) a peak in the increased downwelling located near 55 km.

Figure 2a compares the zonal-mean wind of O_3-Clim and the O_3-Loss when both ZMO and ZAO are included in the model. Figures 2c and 2d show the change in the residual vertical velocity between O_3-Clim and O_3-Loss. As in Manzini et al., we plot the residual vertical velocity as an area-weighted average poleward of 60°N. Each of the Manzini et al. (2003) benchmarks described above is readily identified in our results. Specifically, we obtain 1) a 1–4 m s^{-1} increase in the zonal-mean wind between about 10 and 35 km; 2) a 1–12 m s^{-1} decrease in the zonal-mean wind between about 35 and 70 km; 3) a 0–0.2 mm s^{-1} decrease in the residual vertical velocity between about 10 and 18 km; 4) a 0–1 mm s^{-1} increase in the vertical velocity between about 18 and 65 km; and 5) a peak in the increased downwelling near 51 km. The fact that the benchmarks compare reasonably well with Manzini et al.'s CCM simulations provides confidence that our mechanistic model is able to reproduce the key features of the stratospheric response to ozone depletion. The various radiative and dynamical feedbacks responsible for the changes in the benchmark

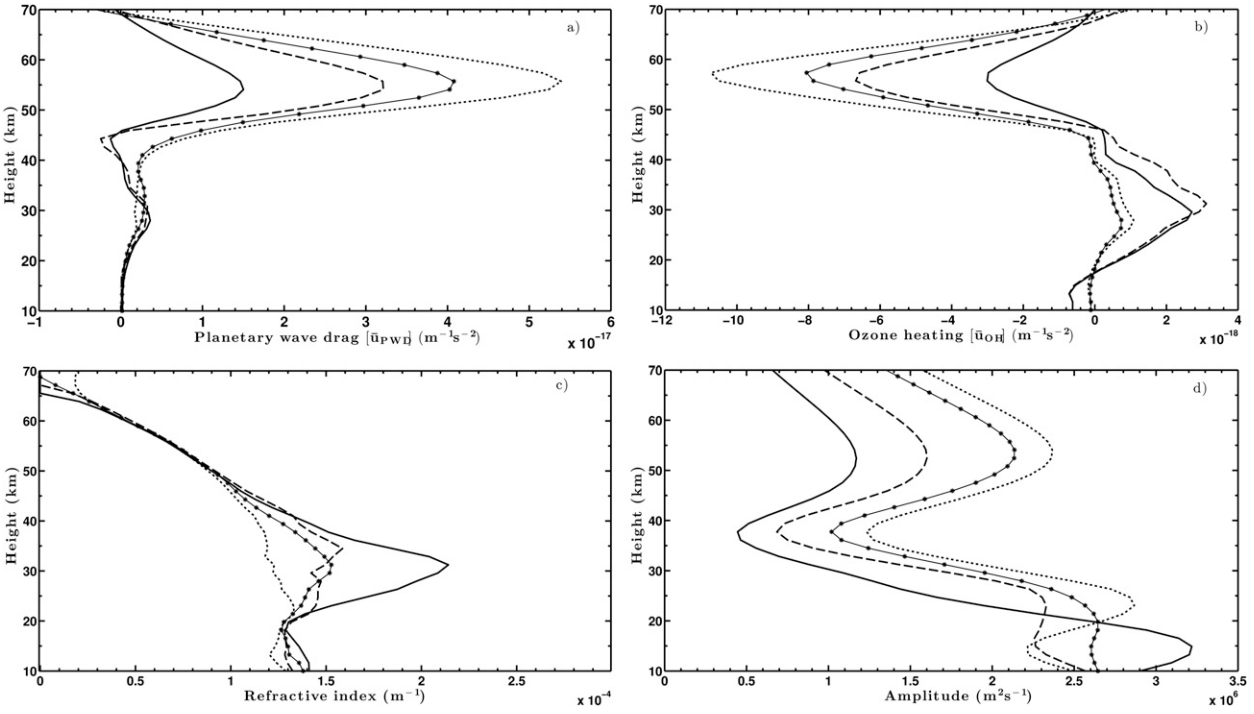

FIG. 3. Steady-state distributions of (a) the planetary wave drag term, (b) the zonal-mean ozone heating term, (c) the refractive index, and (d) the streamfunction amplitude modulus for O_3-Clim with ZAO and ZMO (solid lines), O_3-Clim with ZMO only (dashed lines), O_3-Loss with ZAO and ZMO (solid lines with circles), and O_3-Loss with ZMO only (dotted lines).

wind and downwelling profiles just described are understood as follows.

Our imposed ozone loss perturbation is confined below about 30 km in height and poleward of 60°N. The radiative effect of this ozone perturbation is to cool the high-latitude polar stratosphere, which increases the equator-to-pole temperature gradient. The increased temperature gradient is manifest as a stronger radiative equilibrium polar vortex (see section 2c and Fig. 1c), which subsequently causes the modeled zonal wind to equilibrate to the stronger polar vortex wind profile seen in Fig. 2a. This effect represents the radiative response of the lower-stratospheric temperatures to ozone loss described in the introduction and in section 2b; the radiative, photochemical, and dynamical responses are made clear by considering the diagnostic equations [Eqs. (40)–(44)] described in section 2d.

Figure 3 shows the variations with altitude of $\overline{u}_{\mathrm{PWD}}$ and $\overline{u}_{\mathrm{OH}}$ in Eq. (40) for the O_3-Clim and O_3-Loss experiments in which both ZMO and ZAO are included. Changes in $\overline{u}_{\mathrm{OH}}$ can be divided into three regions: below about 35 km; between about 35 and 45 km; and between about 45 and 70 km. The strong altitude dependence of $\overline{u}_{\mathrm{OH}}$ reflects the decrease with altitude in the ratio of advective to photochemical time scales. In short, the region below about 35 km (termed the dynamical control region) is controlled primarily by advective transport processes, while the region above about 45 km (termed the photochemical control region) is primarily controlled by photochemical and temperature-dependent production/destruction of ozone. The region between about 35 and 45 km (termed the transition region) is controlled jointly by advective and photochemical processes [see Nathan and Cordero (2007) and Albers and Nathan (2012) for details].

In the lower stratosphere, which is under dynamical control, there is a small decrease in both $\overline{u}_{\mathrm{PWD}}$ and $\overline{u}_{\mathrm{OH}}$ (Figs. 3a and 3b, respectively). Thus the primary driver of the wind speed increase seen below about 30 km in Fig. 2a is a result of the radiative ozone forcing described earlier. In the transition region, $\overline{u}_{\mathrm{PWD}}$ again exhibits minimal change, while $\overline{u}_{\mathrm{OH}}$ becomes larger in the presence of the ozone loss perturbation. Because the ozone loss perturbation is confined to the region below about 30 km, we conclude that the decrease in wind speed observed in the transition region in Fig. 2a is due largely to $\overline{u}_{\mathrm{OH}}$. A comparison of the changes to the individual terms (not shown) in the zonal-mean ozone tendency equation [Eq. (7)] reveals that changes in ZMO production/destruction [Eq. (12)] and ozone flux divergences [the second set of bracketed terms on the RHS of Eq. (7)] contribute in roughly equal parts to the change in $\overline{u}_{\mathrm{OH}}$.

The changes in ZMO production/destruction are the radiative–photochemical feedback response to changes in temperature (see the discussion of temperature-dependent chemistry in section 2c), while the change in ozone flux divergence represents a dynamical feedback response due to ZAO (see pathway P2 described in section 2d).

In contrast to the lower stratosphere, the upper stratosphere and lower mesosphere, which are under photochemical control, show large changes in $\overline{u}_{\mathrm{PWD}}$ and $\overline{u}_{\mathrm{OH}}$. Near 55 km, the $\overline{u}_{\mathrm{PWD}}$ term increases (becomes more positive) by 114% and the $\overline{u}_{\mathrm{OH}}$ term increases (becomes more negative) by 122%. Because $\overline{u}_{\mathrm{OH}}$ becomes larger (more negative), which would increase the wind speed, we conclude that $\overline{u}_{\mathrm{PWD}}$ is the sole driver of the wind speed decrease above about 45 km in Fig. 2a. In isolation, the larger negative value of $\overline{u}_{\mathrm{OH}}$ would produce a stronger upper-stratospheric wind rather than the weaker profile observed in our results. Because $\overline{u}_{\mathrm{PWD}}$ is the dominant term responsible for the upper-stratospheric circulation changes, we next consider how the change in $\overline{u}_{\mathrm{PWD}}$ in the upper stratosphere can be understood by considering how wave propagation and wave damping change in the lower stratosphere.

Equations (41) and (43) together show that $\nabla \cdot F$ (i.e., the $\overline{u}_{\mathrm{PWD}}$ term) is proportional to the product of m_r, $|\psi'|^2$, and m_i. In the discussion below, we measure changes in wave propagation by the lowest-order approximation to the refractive index [Eq. (42)] and we measure changes in wave damping by the streamfunction modulus [Eq. (43)]. As described in section 2d, Albers and Nathan (2012) found that changes in wave propagation and wave damping can be offsetting in the lower stratosphere; the result is that $\nabla \cdot F$ does not change appreciably in the lower stratosphere, but the wave arrives in the upper stratosphere in a sufficiently ''preconditioned'' state to produce large changes in $\overline{u}_{\mathrm{PWD}}$. Figure 2a shows that the increase in wind speed associated with lower-stratospheric ozone loss perturbation is largest between about 16 and 36 km; between these heights wave propagation decreases, as seen in Fig. 3c. The wave amplitude exiting the lower stratosphere, however, is notably larger (~62% larger near 35 km). The importance of the change in wave amplitude is further confirmed by noting that the vertical energy flux (not shown) is about 40%–80% larger between about 35 and 45 km in the presence of the ozone loss perturbation. Thus, although the ozone loss perturbation causes a decrease in vertical wave propagation, the local increase in wave amplitude more than compensates; the net result is the large increase in $\overline{u}_{\mathrm{PWD}}$ observed above about 45 km and consequently the warmer and weaker upper-stratospheric and lower-mesospheric polar vortex.

The ozone-induced changes in $\nabla \cdot F$ also cause changes in downwelling, as stated in Eq. (44) and shown in Figs. 2c and 2d. Our analysis shows a slight decrease in downwelling below about 20 km, which is due to the decrease in both wave propagation and wave amplitude, as seen in Figs. 3c and 3d, respectively. The increase in downwelling above about 20 km, however, is due solely to the increase in wave amplitude; this is verified by noting that wave propagation is either smaller or nearly the same above about 20 km in both the O_3-Clim and O_3-Loss experiments (Fig. 3c).

The response of the zonal-mean circulation to the ozone loss perturbation when only ZMO is included in the model (i.e., ZAO is suppressed) is qualitatively different in several important ways. Figure 2b shows the zonal wind response for O_3-Clim and O_3-Loss when ZAO is suppressed. Although the magnitude of the wind response within the lower stratosphere is nearly identical ($\sim$1–4 m s^{-1}) for the O_3-Clim and O_3-Loss experiments, the wind response in the upper stratosphere becomes noticeably weaker ($\sim$1–8 m s^{-1}). The fact that the wind response in the lower stratosphere remains relatively unchanged when ZAO is suppressed is not surprising, because as pointed out earlier, the radiative effects of the ozone loss perturbation predominantly drive the lower-stratospheric wind response. In addition to the change in wind speed, the height of the transition between the stronger winds versus the weaker winds is also markedly different. Indeed, a comparison of Figs. 2a and 2b shows that the upper-stratospheric wind response extends about 8 km lower when ZAO is included.

ZAO also affects the residual vertical velocity [Eq. (44)]. Figures 2c and 2d shows that suppressing ZAO weakens the response of the residual vertical velocity. In the lower stratosphere, the vertical velocity is only slightly weaker, while in the upper stratosphere, the vertical velocity response to the ozone loss is about 25% weaker. In addition, the transition from decreased to increased downwelling shifts upward from about 18 to 28 km (Fig. 2d); likewise, the height of the local maximum in downwelling shifts upward from about 50 to 52 km.

ZAO has two important effects on the zonal-mean circulation. First, including ZAO produces a weaker and warmer stratospheric polar vortex above the region of the ozone loss perturbation than occurs when only ZMO is included in the model. Second, by extending the height of the weaker, warmer polar vortex downward and increasing the strength of the downwelling, ZAO provides a top-down negative dynamical feedback response to the radiative cooling effects of the initial, lower-stratospheric ozone loss perturbation. Each of these changes can be attributed to changes in $\overline{u}_{\mathrm{PWD}}$ and $\overline{u}_{\mathrm{OH}}$.

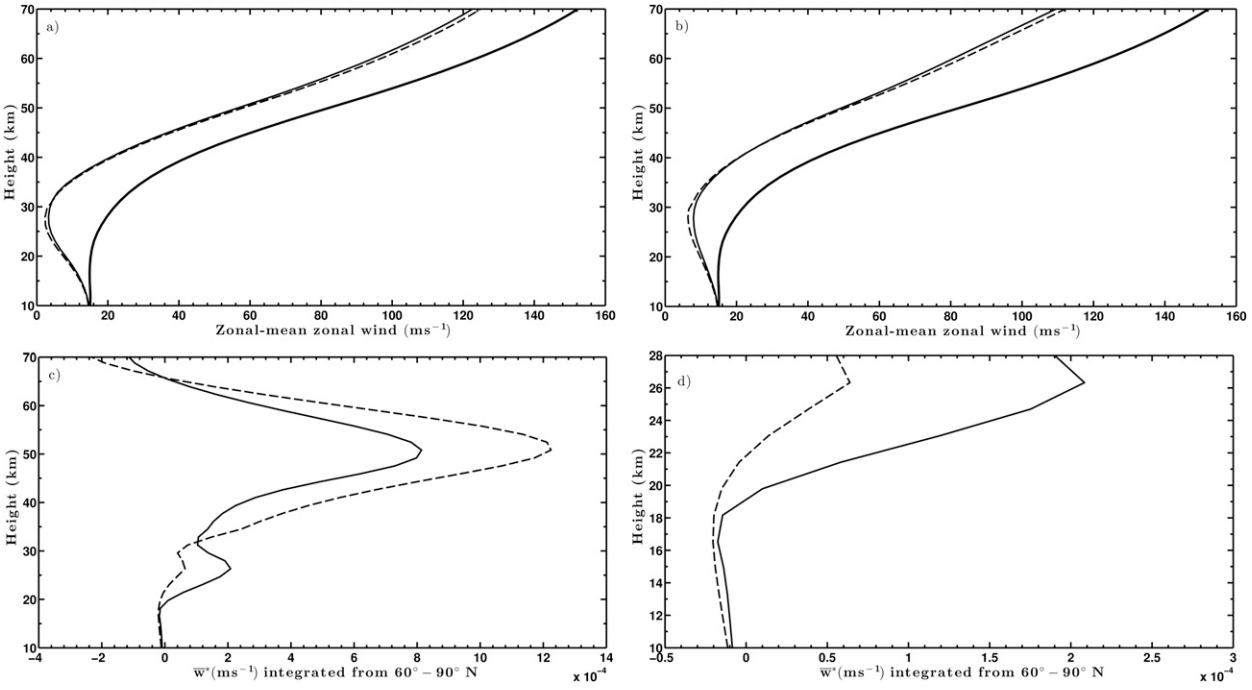

FIG. 4. Steady-state zonal-mean zonal wind for O_3-Clim (solid line) and O_3-Recov (dashed line) when (a) ZAO and ZMO are included in the model and (b) only ZMO is included in the model. The thick solid line denotes the radiative equilibrium zonal-mean zonal wind. (c),(d) The difference (O_3-Clim minus O_3-Recov) in the area-integrated residual vertical velocity when ZAO and ZMO are included in the model (solid line) and when only ZMO is included in the model (dashed line). The vertical axis of (d) is enlarged in order to show detail in the lowermost stratosphere.

In the upper stratosphere and lower mesosphere, ZAO increases the magnitude of the change in $\overline{u}_{\mathrm{PWD}}$ (cf. the difference between the solid and dashed lines versus the solid-circle and dotted lines in Fig. 3a); the change represents a 114% increase near 55 km when ZAO is included versus a 32% increase when only ZMO is included. The change in $\overline{u}_{\mathrm{PWD}}$ is the primary contributor to the more robust weakening of the upper-stratospheric and lower-mesospheric portion of the polar vortex (cf. Figs. 2a and 2b) and to the increase in downwelling observed everywhere above about 20 km (Figs. 2c and 2d).

In the middle-stratosphere transition region, ZAO increases the magnitude of the $\overline{u}_{\mathrm{OH}}$ term via the inclusion of ozone flux convergences; this contributes to both increasing the magnitude of the zonal wind change and to lowering the transition between the increased wind speeds in the upper stratosphere versus the decreased wind speeds in the lower stratosphere.

2) LOWER-STRATOSPHERIC OZONE RECOVERY

To ease comparison of the ozone loss results of the previous section with the ozone recovery results of this section, we present the same set of diagnostics that were used in section 3a when comparing O_3-Clim and O_3-Recov. Figure 4a compares the zonal-mean wind of O_3-Clim and the O_3-Recov, while Figs. 4c and 4d show the change in the residual vertical velocity between O_3-Clim and O_3-Recov for the experiment where both ZMO and ZAO are included (solid and dashed lines in Figs. 4c and 4d). The change in the zonal wind represents a slightly weaker polar vortex in the lower stratosphere ($\sim 1\,\mathrm{m\,s^{-1}}$) and a slightly stronger polar vortex in the upper stratosphere and lower mesosphere ($\sim 3\,\mathrm{m\,s^{-1}}$). The change in the area-weighted average residual vertical velocity poleward of 60°N varies between 0 and $-0.14\,\mathrm{mm\,s^{-1}}$ between 10 and 20 km (an increase in downwelling) and between 0 and $-0.41\,\mathrm{mm\,s^{-1}}$ between 20 and 70 km (a decrease in downwelling); the local maxima in downwelling are located near 18 and 50 km, respectively.

In the lower stratosphere, the model produces the expected radiative response to the polar ozone recovery perturbation; that is, the wind profile of O_3-Recov represents a slightly weaker polar vortex that is associated with the decreased meridional temperature gradient. We again assess the role of dynamical feedbacks in producing the circulation changes by considering the $\overline{u}_{\mathrm{PWD}}$ and $\overline{u}_{\mathrm{OH}}$ terms of Eq. (40).

Figures 5a and 5b show the change in $\overline{u}_{\mathrm{PWD}}$ and $\overline{u}_{\mathrm{OH}}$ for O_3-Clim and O_3-Recov. Below about 25 km, $\overline{u}_{\mathrm{PWD}}$

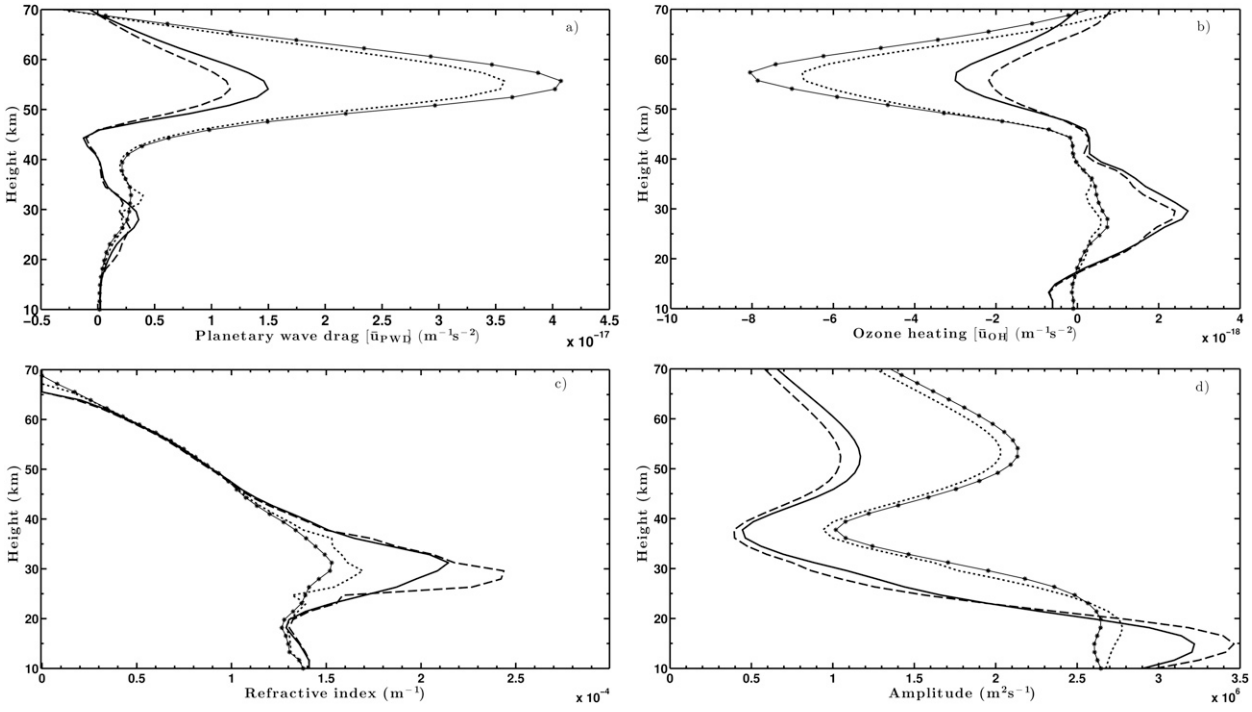

FIG. 5. Steady-state distributions of (a) the planetary wave drag term, (b) the zonal-mean ozone heating term, (c) the refractive index, and (d) the streamfunction amplitude modulus for O_3-Clim with ZAO and ZMO (solid lines), O_3-Clim with ZMO only (dashed lines), O_3-Recov with ZAO and ZMO (solid lines with circles), and O_3-Recov with ZMO only (dotted lines).

and $\overline{u}_{OH}$ have changed only minimally in response to the ozone recovery perturbation, thus the response of the wind in the lowermost stratosphere is largely a result of the radiative effects of ozone recovery. Between about 25 and 40 km, however, $\overline{u}_{OH}$ decreases in response to the imposed ozone recovery. Moreover, the change in $\overline{u}_{OH}$ is primarily due to ZAO; this can be verified by comparing the solid and dashed lines for O_3-Recov with both ZMO and ZAO included versus the solid-circle and dashed lines for O_3-Recov with only ZMO included. The change in $\overline{u}_{OH}$ due to ZAO has two important effects on the zonal-mean wind. First, between about 25 and 35 km the decrease in $\overline{u}_{OH}$ offsets some of the increased radiative heating associated with ozone recovery; this is verified by noting that the ozone recovery-induced zonal-mean wind change is weaker in the experiment that includes both ZAO and ZMO (cf. Figs. 4a and 4b). Second, the transition from the weaker polar vortex to a stronger polar vortex occurs about 10 km lower when ZAO is included in the model. In the upper stratosphere and lower mesosphere, virtually all of the change in zonal wind is due to changes in $\overline{u}_{PWD}$. However, as in the O_3-Loss experiment, changes in wave propagation and wave damping in the lower-stratosphere and middle-atmosphere transition region play an important role in determining the change in $\overline{u}_{PWD}$ in the upper stratosphere and lower mesosphere; we explore this topic in more detail in the next section.

b. Discussion

The previous two sections identified the physics that communicates lower-stratospheric ozone loss throughout the stratosphere and lower mesosphere. We now describe how our results explain recent observational and modeling studies that address the effect of ozone loss and recovery on the Brewer–Dobson circulation (BDC) and the strength of the NH polar vortex. We focus on the results of the ozone loss experiment, but note that the radiative, photochemical, and dynamical feedbacks discussed are similar in nature (though opposite in sign) to the ozone recovery experiment.

The BDC is the global stratospheric meridional circulation that transports chemical species poleward from the tropics via a combination of mean mass transport and quasi-horizontal mixing (Plumb 2002; Shepherd 2007; Birner and Bönisch 2011). The zonal-mean mass transport represents a Lagrangian circulation consisting of rising air in the tropics, poleward air transport, and sinking air in midlatitudes and the polar regions. This circulation is approximated by the TEM residual-mean meridional circulation, or simply the residual circulation (Andrews et al. 1987).

The rising and sinking motion of the residual circulation consists of two branches: a shallow branch within the lower stratosphere and a deep branch within the upper stratosphere and mesosphere (Birner and Bönisch 2011; Bönisch et al. 2011). The two branches of the BDC are driven by a broad spectrum of waves, spanning planetary-scale waves to small-scale gravity waves. Thus changes in the flux of vertical wave activity, whether caused by changes in propagation, damping, or a combination of both, will modulate the vigor of the BDC.

One of the mechanisms responsible for the increased wave-driven mass flux, which is reproduced in all of the CCMs, is the acceleration of the subtropical jets due to climate change. As the subtropical jet accelerates, the critical layer for wave breaking, which determines the height of orographic gravity and Rossby wave forcing, moves upward (Shepherd and McLandress 2011). However, changing the height of this critical layer is only capable of controlling wave forcing within the subtropics. And while this region is indeed important because changes in the strength of the BDC must be driven via changes in wave forcing within the ''turnaround latitudes'' (Rosenlof 1995), the location of the turnaround latitudes themselves are determined jointly by a wider range of wave forcing that extends to lower and higher latitudes (Zhou et al. 2012). Indeed observational studies have indicated that wave forcing in the extratropical ''surf zone'' also plays a significant role in driving changes in the BDC on a variety of times scales (Zhou et al. 2012). Thus determining the relative strengths of each of these wave forcings will be critical for predicting both the latitudinal distribution of upwelling and downwelling and the spatial distribution of stratospheric ozone (Zhou et al. 2012). Unfortunately, research examining the stratospheric wave response to changes in ozone and GHGs has produced conflicting results.

For example, several modeling studies (Butchart and Scaife 2001; Eichelberger and Hartmann 2005; Eyring et al. 2006; McLandress and Shepherd 2009; Calvo and Garcia 2009) have found that increasing GHG abundance and ozone depletion combine to produce an increase in wave activity entering the stratosphere; the increase in wave activity in turn, drives an increase in the tropical upward mass flux along the shallow branch of the BDC. The reasons proposed for the increase in the strength of the BDC, however, vary considerably. McLandress and Shepherd (2009) found that a combination of large-scale planetary (both stationary and transient) and synoptic-scale waves account for much of the modeled increase in the strength of the BDC. Moreover, McLandress and Shepherd also found that the increase in wave activity is due to increased wave generation in the troposphere rather than changes in vertical wave propagation within the upper troposphere–lower stratosphere. In contrast, Garcia and Randel (2008) and Calvo and Garcia (2009) find that increases in upward tropical mass flux along the shallow branch of the BDC are due to increased vertical propagation and dissipation of planetary waves in the subtropics. Unfortunately, verifying the modeling results just described is difficult owing to the fact that trends in the BDC are noisy and have error bounds that are as large as the amplitude of the trends themselves (Baldwin et al. 2007; Engel et al. 2009). Therefore, determining whether the BDC will accelerate due to changes in wave generation and dissipation or wave propagation remains unresolved (WMO 2011).

While the studies listed above agree that the upward tropical mass flux along the shallow branch of the BDC should accelerate in response to changes in ozone and increasing GHG abundances, the predicted change in upwelling in the tropics must be balanced by increased downwelling in the extratropics and polar regions (Holton et al. 1995). Our goal is to provide an explanation of the physics of these circulation changes, detailing how changes in lower-stratospheric ozone modulate the propagation and damping characteristics of stationary planetary waves during the NH late winter and early spring seasons. In doing so, we provide insight into the physics of how ozone loss and recovery will affect the strength of the Arctic polar vortex and polar downwelling along both the shallow and deep branches of the BDC.

Modeling and observational studies have demonstrated that polar lower-stratospheric temperatures cooled in response to ozone depletion and increasing levels of GHGs between roughly 1980 and 2000 (Randel and Wu 1999; Ramaswamy et al. 2001; Shindell et al. 2001). This lower-stratospheric cooling was accompanied by a reduction in vertical wave propagation and a reduction in the vertical component of the EP flux (Hu and Tung 2003; Coy et al. 1997). Several recent CCM studies corroborate this view. For example, Oman et al. (2009) found that lower-stratospheric ozone depletion during NH winter caused an increase in the meridional temperature gradient and a corresponding strengthening of the Arctic polar vortex (see Oman et al.'s Figs. 10b and 10d, respectively). The change in the polar vortex was accompanied by a decrease in the lower-stratospheric vertical EP flux between 30° and 75°N and a decrease in downwelling between 60°N and 90° (see Oman et al.'s Figs. 10f and 10h, respectively). Thus, the results of Oman et al. are consistent with those of Manzini et al. (2003) outlined in section 3a. In combination, these observational and modeling results show that the response of the extratropical and polar lower stratosphere

to lower-stratospheric ozone depletion is consistent with our results, including a strengthening of the lower-stratospheric polar vortex (Fig. 2a), a decrease in vertical wave propagation (Fig. 3c), a decrease in vertical energy flux between about 10 and 30 km (not shown), and a decrease in the residual vertical velocity along the shallow branch of the BDC (Figs. 2c and 2d).

The response of the upper stratosphere and lower mesosphere to lower-stratospheric ozone loss in our results is also consistent with the results of Manzini et al. including a weakening of the upper-stratospheric polar vortex (Fig. 2a), an increase in the vertical energy flux above about 35 km (not shown), and an increase in the residual vertical velocity along the deep branch of the BDC (Figs. 2c and 2d). The changes in the upper stratosphere, however, are at first puzzling. This is because the only difference between the O_3-Clim and O_3-Loss experiments is an imposed ozone loss perturbation below about 30 km, yet the largest change in the zonal-mean circulation and planetary wave drag occur in the upper stratosphere. In section 3a(2) we used an expression for the ozone-modified planetary wave drag [Eq. (41)] (Nathan and Cordero 2007; Albers and Nathan 2012) to explain how changes in wave propagation and wave damping combine to alter the residual vertical velocity and the zonal-mean wind in a qualitatively different sense in the upper versus lower stratosphere. We now offer an explanation for the inverse relationship between wave propagation and wave amplitude observed in both the O_3-Loss and O_3-Recov sets of experiments.

Albers and Nathan (2012) showed that in the lower stratosphere, regions of decreased wave amplitude corresponded with regions of increased vertical wave propagation (see their Fig. 5). This can be most easily understood by considering the ozone-modified, WKB planetary wave amplitude modulus in the limit of small damping [see Nathan et al. (2011)'s Eq. (19)]:

$$|A| \propto \frac{\sigma}{\sqrt{m_0}} \exp\left(- \int_0^{z'} m_{1i}\, dz \right), \tag{45}$$

where A is the WKB wave amplitude, m_0 is the (real) refractive index [Eq. (42)], σ is a constant determined from the lower boundary condition, and m_{1i} represents wave damping. In Eq. (45), m_{1i} is a function of ZAO, ZMO, and Newtonian cooling. Below about 35 km, damping due to ozone and Newtonian cooling are relatively small [see Figs. 3a and 3c of Nathan and Li (1991)]. Thus if we consider the flow to be nearly adiabatic in this region ($m_{1i} \to 0$), then we find that wave amplitude and wave propagation are inversely proportional in the lower stratosphere. While this inverse relationship does not hold throughout the whole lower stratosphere in our results, most notably near the lower boundary in Figs. 3c, 3d, 4c, and 4d, it nevertheless accounts for the changes in wave amplitude and wave propagation between about 20 and 40 km, which is responsible for producing the significant changes in planetary wave drag, the residual vertical velocity, and the zonal-mean wind in the upper stratosphere and lower mesosphere in both O_3-Loss and O_3-Recov.

In addition to the wave amplitude–wave propagation relationship just described, changes in meridional planetary wave propagation and gravity wave drag—processes not accounted for in our model setup—may also play a role in the zonal-mean wind and residual circulation changes found in Manzini et al. (2003) and Oman et al. (2009). Specifically, an increase in poleward refraction of planetary waves due to changes in the background zonal-mean wind as well as gravity wave drag could also cause an increase in EP flux divergence and an associated change in the zonal-mean wind and residual circulation. A more complex model that incorporates two-dimensional wave propagation and gravity wave drag will be needed in order to assess the relative importance of ozone-induced wave-amplitude increases versus increased poleward wave refraction and gravity wave drag for driving the ozone-modified circulation responses examined in this study.

4. Conclusions

The high-latitude lower stratosphere cooled in response to ozone depletion and increasing GHG abundances between 1960 and 2000 (WMO 2011). Over the course of the twenty-first century, ozone is expected to recover as concentrations of ODSs decrease in association with the Montreal Protocol. The recovery of ozone, however, is not expected to proceed uniformly across all latitudes and heights (Shepherd 2008; Li et al. 2009). The complicated spatial evolution in the predicted ozone recovery is expected to occur as a result of many factors, including changes in ozone transport associated with the intensification of the BDC (Eyring et al. 2006; Shepherd 2008; Li et al. 2009) and increased upper-stratospheric ozone production due to GHG-induced upper-stratospheric cooling. In particular, because the BDC transports ozone poleward from the equatorial region, the stronger circulation is expected to produce what Shepherd (2008) has termed an ozone ''super recovery'' in the extratropics and a ''sub recovery'' in the tropics. Moreover, as GHG abundances increase and produce a decrease in stratospheric temperatures, the decrease in temperature will accelerate upper-stratospheric ozone recovery due to the temperature dependence of

the gas-phase ozone loss reactions (Barnett et al. 1975). Because ozone recovery and increases in GHG abundance will be occurring simultaneously, attribution of their respective roles in climate change will require a detailed understanding of how each process will affect stratospheric dynamics. Unfortunately, the effects of ozone loss and recovery versus the effects of increasing GHG abundances on stratospheric dynamics are currently not well understood (WMO 2011).

In this study we have used a mechanistic chemistry–dynamical model to show how the qualitatively different lower- versus upper-stratospheric circulation response to ozone depletion, which have been reported in observations (Coy et al. 1997; Hu and Tung 2003) and reproduced in CCM models (Manzini et al. 2003; Oman et al. 2009), can be explained via a combination of changes in direct ozone–radiative heating and dynamical feedbacks. In the lowermost stratosphere (~10–20 km), our model responds to springtime NH high-latitude ozone depletion by causing a decrease in lower-stratospheric temperatures, which is primarily due to the decrease in ozone radiative heating and is a well-known response of the springtime lower stratosphere to ozone depletion (Ramaswamy et al. 2001; WMO 2011). The decrease in polar temperature also causes an increase in the meridional temperature gradient and, via thermal wind, an increase in the strength of the polar vortex and a subsequent decrease in vertical wave propagation. In this same region, planetary wave drag also decreases, which causes a decrease in residual circulation downwelling between 60° and 90°N. This represents the dynamical feedback response of stationary planetary waves to ozone depletion in the lowermost stratosphere. Between 20 and 40 km, however, the dynamical feedback response to ozone depletion is significantly different.

As planetary waves propagate upward between 20 and 40 km, vertical wave propagation decreases due to decreased polar radiative heating associated with ozone depletion. However, the ozone depletion also causes a large increase in wave amplitude and a 40%–80% increase in vertical energy flux. This is the ''preconditioning'' effect of ozone on vertically propagating planetary waves found by Albers and Nathan (2012). Consequently, the planetary waves leave the ozone loss region with a substantially larger amplitude. This has three important effects on the upper stratosphere and lower mesosphere, including an increase in planetary wave drag, an increase in residual circulation downwelling between 60° and 90°N, and a weaker polar vortex. Interestingly, this result provides an explanation for a potentially important dynamical feedback first proposed by Manzini et al. (2003) in a CCM study.

Specifically, Manzini et al. (2003) propose that ozone depletion and increased GHGs abundances may cause an increase in planetary and gravity wave–driven residual circulation downwelling in the NH high latitudes during spring. The result is a negative dynamical feedback (due to adiabatic warming) from above that may help to offset the decrease in lower-stratospheric temperatures associated with decreased radiative heating from ozone depletion. Manzini et al. (2003) ascribe the change in gravity wave driving to differential filtering of eastward- versus westward-propagating waves as the waves pass upward through the stronger lower-stratospheric polar vortex that resulted from ozone depletion. Smith et al. (2010) observe a similar result in the SH. However, because the increased strength of the lower-stratospheric polar vortex causes a decrease in the vertical propagation of planetary waves, a similar argument cannot explain the increased planetary wave–driven downwelling or the decrease in the strength of the polar vortex seen in the upper stratosphere. Indeed, Manzini et al. were unable to provide a concrete rationale for the increase in upper-stratospheric downwelling observed in their study. Our results provide a physically based rationale for Manzini et al.'s results; that is, we show that as the background distributions of wind and temperature change due to the radiative effects of ozone depletion, accurate representations of both wave propagation and wave damping within the lower stratosphere are crucial to diagnosing and explaining the stratospheric-wide dynamical response.

Overall we find that ozone depletion causes dynamical feedbacks that contribute to weakening downwelling along the shallow branch of the BDC, increasing downwelling along the deep branch of the BDC, and weakening the strength of the Arctic polar vortex in the upper stratosphere and lower mesosphere. In contrast, as ozone begins to recover over the course of the twenty-first century, our results suggest that dynamical feedbacks will contribute to strengthening the downwelling along the shallow branch of the BDC, weakening the downwelling along the deep branch of the BDC, and strengthening of the Arctic polar vortex in the upper stratosphere and lower mesosphere.

In addition, we find that zonally asymmetric ozone (ZAO) modulates downwelling in both the ozone loss and ozone recovery experiments. The effect of including ZAO in the ozone loss and ozone recovery experiments is strikingly different. In the ozone loss experiment the downwelling is about 35% stronger. In sharp contrast, in the ozone recovery experiment the downwelling is about 34% weaker. Although ozone depletion and recovery precondition planetary waves regardless of whether ZAO is included in the model, the effect is significantly

stronger in the model runs that include ZAO. Thus when compared to CCMs, GCMs without interactive stratospheric chemistry will underestimate the increase in downwelling associated with ozone depletion and overestimate the decrease in downwelling associated with ozone recovery.

The above results may be helpful for researchers attempting to diagnose the relative importance of increases in GHG abundances versus ozone loss and recovery for driving future changes in the BDC. For example, Austin et al. (2007) suggest that both ozone depletion and increased GHG abundances contributed to accelerating the BDC between 1980 and 2000. Likewise, Austin et al. suggest that ozone recovery will likely temper the GHG-induced BDC acceleration (Butchart and Scaife 2001) in the future. Yet Austin et al. also suggest that attributing BDC changes specifically to changes ozone is difficult because observations and most CCM studies also include additional climate variables (e.g., changes in SST and GHG abundances) that will also modify the BDC. Nevertheless, within the middle and upper stratosphere, where we find the largest change in planetary wave–driven downwelling due to variations in ozone, our results largely support the hypothesis of Austin et al. regarding the buffering effect of ozone recovery on any future acceleration of the BDC.

Finally, our results highlight the benefits of using a hierarchical modeling approach when conducting climate research. One of the primary difficulties in understanding and attributing changes in stratospheric and tropospheric climate to various climate forcings is that the CCMs used to study these forcings simulate hundreds of radiative, chemical, and dynamical processes. The result of simulating all of these processes at once is that delineating the relative importance of individual climate forcings becomes a formidable problem at high computational expense. By using an idealized model that includes only the most relevant physical processes, such as the one used in this study, the mechanisms responsible for communicating the effects of each individual climate forcing can be studied in isolation and their physics more easily understood. The results of these simplified simulations can then be used as a guide in which to interpret and understand more complex CCM simulations and observational datasets.

Acknowledgments. This work was supported in part by NASA's Living with a Star, Targeted Research and Technology Program (TRN and ECC), Grant LWS04-0025-0108, NASA Grant NNH08AI67I (TRN), and NSF Grant ATM-0733698 (TRN).

REFERENCES

Albers, J. R., and T. R. Nathan, 2012: Pathways for communicating the effects of stratospheric ozone to the polar vortex: Role of zonally asymmetric ozone. *J. Atmos. Sci.,* **69,** 785–801.

Andrews, D. G., J. R. Holton, and C. B. Leovy, 1987: *Middle Atmosphere Dynamics.* Academic Press, 489 pp.

Austin, J., J. Wilson, and H. Vömel, 2007: Evolution of water vapor concentrations and stratospheric age of air in coupled chemistry–climate model simulations. *J. Atmos. Sci.,* **64,** 905–921.

Baldwin, M., and Coauthors, 2007: Climate–ozone connections. Scientific assessment of ozone depletion: 2006, Global Ozone Research and Monitoring Project Rep. 50, WMO, 5.1–5.49.

Barnett, J. J., J. T. Houghton, and J. A. Pyle, 1975: The temperature dependence of the ozone concentration near the stratopause. *Quart. J. Roy. Meteor. Soc.,* **101,** 245–257.

Birner, T., and H. Bönisch, 2011: Residual circulation trajectories and transit times into the extratropical lowermost stratosphere. *Atmos. Chem. Phys.,* **11,** 817–827.

Bönisch, H., A. Engel, T. Birner, P. Hoor, D. W. Tarasick, and E. A. Ray, 2011: On the structural changes in the Brewer–Dobson circulation after 2000. *Atmos. Chem. Phys.,* **11,** 3937–3948.

Brasseur, G. P., and M. A. Hitchman, 1988: Stratospheric response to trace gas perturbations: Changes in ozone and temperature distributions. *Science,* **240,** 634–637.

——, and S. Solomon, 2005: *Aeronomy of the Middle Atmosphere: Chemistry and Physics of the Stratosphere and Mesosphere.* Springer, 644 pp.

Butchart, N., and A. A. Scaife, 2001: Removal of chlorofluorocarbons by increased mass exchange between the stratosphere and troposphere in a changing climate. *Nature,* **410,** 799–802.

Calvo, N., and R. R. Garcia, 2009: Wave forcing of the tropical upwelling in the lower stratosphere under increasing concentrations of greenhouse gases. *J. Atmos. Sci.,* **66,** 3184–3196.

Charney, J., and P. Drazin, 1961: Propagation of planetary-scale disturbances from the lower into the upper atmosphere. *J. Geophys. Res.,* **66,** 83–109.

Coy, L., E. R. Nash, and P. A. Newman, 1997: Meteorology of the polar vortex: Spring 1997. *Geophys. Res. Lett.,* **24,** 2693–2696.

Craig, C. A., and G. Ohring, 1958: The temperature dependence of ozone radiational heating rates in the vicinity of the mesopeak. *J. Meteor.,* **15,** 59–62.

Eichelberger, S. J., and D. L. Hartmann, 2005: Changes in the strength of the Brewer-Dobson circulation in a simple AGCM. *Geophys. Res. Lett.,* **32,** L15807, doi:10.1029/2005GL022924.

Engel, A., and Coauthors, 2009: Age of stratospheric air unchanged within uncertainties over the past 30 years. *Nat. Geosci.,* **2,** 28–31.

Eyring, V., and Coauthors, 2006: Assessment of temperature, trace species, and ozone in chemistry-climate model simulations of the recent past. *J. Geophys. Res.,* **111,** D22308, doi:10.1029/2006JD007327.

Garcia, R. R., and W. J. Randel, 2008: Acceleration of the Brewer–Dobson circulation due to increases in greenhouse gases. *J. Atmos. Sci.,* **65,** 2731–2739.

Haigh, J., and J. Pyle, 1982: Ozone perturbation experiments in a two-dimensional circulation model. *Quart. J. Roy. Meteor. Soc.,* **108,** 551–574.

Holton, J. R., 2004: *An Introduction to Dynamic Meteorology.* 4th ed. Academic Press, 535 pp.

——, P. H. Haynes, M. E. McIntyre, A. R. Douglass, R. B. Rood, and L. Pfister, 1995: Stratosphere–troposphere exchange. *Rev. Geophys.,* **33,** 403–439.

Hu, Y., and K.-K. Tung, 2003: Possible ozone-induced long-term changes in planetary wave activity in late winter. *J. Climate,* **16,** 3027–3038.

Jin, J., and Coauthors, 2006: Severe arctic ozone loss in the winter 2004/2005: Observations from ACE-FTS. *Geophys. Res. Lett.,* **33,** L15801, doi:10.1029/2006GL026752.

Keating, G., L. Chiou, and N. Hsu, 1996: Improved ozone reference models for the COSPAR international reference atmosphere. *Adv. Space Research,* **18,** 11–58.

Li, F., R. S. Stolarski, and P. A. Newman, 2009: Stratospheric ozone in the post-CFC era. *Atmos. Chem. Phys.,* **9,** 2207–2213.

Lindzen, R., and R. Goody, 1965: Radiative and photochemical processes in mesospheric dynamics. Part I: Models for radiative and photochemical processes. *J. Atmos. Sci.,* **22,** 341–348.

Manney, G. L., and Coauthors, 2011: Unprecedented Arctic ozone loss in 2011. *Nature,* **478,** 469–475.

Manzini, E., B. Steil, C. Brühl, M. A. Giorgetta, and K. Krüger, 2003: A new interactive chemistry-climate model: 2. Sensitivity of the middle atmosphere to ozone depletion and increase in greenhouse gases and implications for recent stratospheric cooling. *J. Geophys. Res.,* **108,** 4429, doi:10.1029/2002JD002977.

McLandress, C., and T. G. Shepherd, 2009: Simulated anthropogenic changes in the Brewer–Dobson circulation, including its extension to high latitudes. *J. Climate,* **22,** 1516–1540.

Metz, B., and Coauthors, Eds., 2005: Safeguarding the ozone layer and the global climate system: Issues related to hydrofluorocarbons and perfluorocarbons. Cambridge University Press, 488 pp.

Nathan, T. R., and L. Li, 1991: Linear stability of free planetary waves in the presence of radiative–photochemical feedbacks. *J. Atmos. Sci.,* **48,** 1837–1855.

——, and E. C. Cordero, 2007: An ozone-modified refractive index for vertically propagating planetary waves. *J. Geophys. Res.,* **112,** D02105, doi:10.1029/2006JD007357.

——, J. R. Albers, and E. C. Cordero, 2011: Role of wave–mean flow interaction in sun–climate connections: Historical overview and some new interpretations and results. *J. Atmos. Sol.-Terr. Phys.,* **73,** 1594–1605.

Newman, P. A., E. R. Nash, and J. E. Rosenfield, 2001: What controls the temperature of the Arctic stratosphere during the spring? *J. Geophys. Res.,* **106** (D17), 19 999–20 010.

Oman, L., D. W. Waugh, S. Pawson, R. S. Stolarski, and P. A. Newman, 2009: On the influence of anthropogenic forcings on changes in the stratospheric mean age. *J. Geophys. Res.,* **114,** D03105, doi:10.1029/2008JD010378.

Pawson, S., and B. Naujokat, 1999: The cold winters of the middle 1990's in the northern lower stratosphere. *J. Geophys. Res.,* **104,** 14 209–14 222.

Plumb, R. A., 2002: Stratospheric transport. *J. Meteor. Soc. Japan,* **80,** 793–809.

Ramaswamy, V., and Coauthors, 2001: Stratospheric temperature trends: Observations and model simulations. *Rev. Geophys.,* **39,** 71–122.

Randel, W. J., and F. Wu, 1999: Cooling of the Arctic and Antarctic polar stratospheres due to ozone depletion. *J. Climate,* **12,** 1467–1479.

Rex, M., and Coauthors, 2006: Arctic winter 2005: Implications for stratospheric ozone loss and climate change. *Geophys. Res. Lett.,* **33,** L23808, doi:10.1029/2006GL026731.

Rosenlof, K. H., 1995: Seasonal cycle of the residual mean meridional circulation in the stratosphere. *J. Geophys. Res.,* **100,** 5173–5191.

Shepherd, T. G., 2007: Transport in the middle atmosphere. *J. Meteor. Soc. Japan,* **85B,** 165–191.

——, 2008: Dynamics, stratospheric ozone, and climate change. *Atmos.–Ocean,* **46,** 117–138.

——, and A. I. Jonsson, 2008: On the attribution of stratospheric ozone and temperature changes to changes in ozone-depleting substances and well-mixed greenhouse gases. *Atmos. Chem. Phys. Discuss.,* **7,** 12 327–12 347.

——, and C. McLandress, 2011: A robust mechanism for strengthening of the Brewer–Dobson circulation in response to climate change: Critical-layer control of subtropical wave breaking. *J. Atmos. Sci.,* **68,** 784–797.

Shindell, D. T., G. A. Schmidt, R. L. Miller, and D. Rind, 2001: Northern Hemisphere winter climate response to greenhouse gas, ozone, solar, and volcanic forcing. *J. Geophys. Res.,* **106,** 7193–7210.

Smith, A. K., R. R. Garcia, D. R. Marsh, D. E. Kinnison, and J. H. Richter, 2010: Simulations of the response of mesospheric circulation and temperature to the Antarctic ozone hole. *Geophys. Res. Lett.,* **37,** L22803, doi:10.1029/2010GL045255.

Solomon, S., 1999: Stratospheric ozone depletion: A review of concepts and history. *Rev. Geophys.,* **37,** 275–316.

Thompson, D. W. J., and S. Solomon, 2009: Understanding recent stratospheric climate change. *J. Climate,* **22,** 1934–1943.

Tilmes, S., R. Müller, A. Engel, M. Rex, and J. M. Russel, 2006: Chemical ozone loss in the Arctic and Antarctic stratosphere between 1992 and 2005. *Geophys. Res. Lett.,* **33,** L20812, doi:10.1029/2006GL026925.

WMO, 2011: Scientific assessment of ozone depletion: 2010. Global Ozone Research and Monitoring Project Rep. 52, WMO, 516 pp.

Zhou, T., M. A. Geller, and W. Lin, 2012: An observational study on the latitudes where wave forcing drives Brewer–Dobson upwelling. *J. Atmos. Sci.,* **69,** 1916–1935.